JMEPEG
https://doi.org/10.1007/s11665-025-11055-2

©ASM International
1059-9495/$19.00

ORIGINAL RESEARCH ARTICLE

Nanostructure Evolution and Rupture Mechanisms in Layered Fe-Cr-Ni Alloy under Multiaxial Tensile Deformation: A Molecular Dynamics Study

Arun Kumar, Ashok Kumar, and Sunil Kumar

Submitted: 16 September 2024 / Revised: 5 December 2024 / Accepted: 6 January 2025

This study investigates the rupture mechanism of layered Fe-Cr-Ni alloy under multiaxial tensile deformation using molecular dynamics simulations. The results found that the presence of layered orientation of Fe-Cr-Ni significantly impacts nanovoid formation, growth, and coalescence during multiaxial (uniaxial, biaxial, and triaxial) deformation. During triaxial deformation, nanovoids nucleate early and grow rapidly, leading to material failure, with body-centered cubic structure forming around void surfaces due to strain-induced phase transformations. Biaxial tensile deformation facilitates minor amount of face-centered cubic to body-centered cubic transformations with rectangular and square-shaped stacking faults. Uniaxial tensile deformation produces the highest degree of dislocation interactions, leading to complex defect structures. Our study highlights that the yield stress, dislocation density, surface area, and solid volume vary across different deformation modes. Layered or twin boundaries act as barriers for movement of dislocation, reducing the plasticity and enhancing void nucleation. Our findings provide critical insights into atomic-scale mechanisms driving void formation, phase transformation, and material failure in Fe-Cr-Ni alloys with twin boundaries, contributing to improved material design under multiaxial loading conditions.

Keywords Fe-Cr-Ni alloy, mechanical properties, molecular dynamics simulation, multiaxial tensile deformation, nanovoids, twin boundaries

1. Introduction

Fe-Cr-Ni alloys are a vital component of the 300 series stainless steels (Ref 1, 2) and are commonly used in the nuclear (Ref 3-7), automobile (Ref 7-9), marine (Ref 7, 10, 11), aerospace (Ref 7, 12, 13), chemical and petrochemical industries (Ref 7, 14-17). It shows excellent corrosion resistance high strength, ductility, formability, stability at high temperatures, and non-magnetic properties (Ref 6, 18-23). The incorporation of layered structure or twin boundaries in these alloys significantly improves their mechanical properties, including improved strength, retain ductility (Ref 24), fracture resistance (Ref 25), and performance under high strain rates (Ref 26). The interaction of twin boundaries with dislocations plays a critical role in defining the overall material's strength (Ref 27, 28).

Numerous studies have explored the impact of twin boundaries on the mechanical properties and crystal structures of metals and alloys under uniaxial tensile deformation. These investigations often highlight that increasing twin boundary spacing typically reduces the yield strength showing that increasing twin boundary spacing generally reduces yield strength (Ref 29-35). Experimental studies have also examined multiaxial deformation in metals and alloys (Ref 36-38). For instance, Dong et al. (Ref 39) reported that during multiaxial ratchetting deformation of 316L stainless steel, dislocation patterns develop similar to those in uniaxial deformation, with rapid establishment of dislocation networks and tangles followed by polarized patterns such as dislocation walls and elongated incipient dislocation cells. Qin et al. (Ref 40) demonstrated that the continuum plasticity model precisely predicts the multiaxial mechanical response of DP600 steel and that the microstructural RVE model can effectively capture the macroscopic multiaxial plasticity behavior based on the observed microstructures. Mohr et al. (Ref 41) used a newly developed multiaxial testing method for sheet metal and found that Hill's quadratic yield function with a related flow rule precisely predicts the initial yield behavior of temper-rolled stainless steel 301LN under varying loading conditions.

While many molecular dynamics (MD) simulations have investigated multiaxial deformation of multiple kinds of alloys (Ref 42-44), the exploration of Fe-Cr-Ni alloys under multiaxial tensile deformation remains comparatively underrepresented. Previous MD studies have mainly focused on uniaxial tensile deformation, examining the influence of twin spacing on crystal structure and mechanical properties. For instance, Zhang et al. (Ref 45) observed that in an Al0.1CoCrFeNi high-entropy alloy, larger twin spacing led to reduced yield strength during uniaxial deformation. Similarly, Yang et al. (Ref 29) reported that increased twin spacing in copper nanowires resulted in a transition from strain hardening to nearly constant flow stress,

Arun Kumar and **Ashok Kumar**, National Institute of Technology, Jamshedpur 831014, India; and **Sunil Kumar**, CSIR-National Metallurgical Laboratory, Jamshedpur 831007, India. Contact e-mails: sunil@nml.res.in and suniliitd14@gmail.com.

Published online: 01 April 2025

reducing peak stress and surface roughness due to crystal reorientation.

In our earlier work (Ref 46-50), we analyzed the structural transformations in various metallic and polymeric materials under multiaxial tensile deformation using MD simulations. These studies revealed a two-stage transformation process: from BCC to FCC, followed by a reverse transformation to BCC. Additionally, the nucleation, growth, and coalescence of nanovoids were systematically characterized.

Despite advancements in experimental and simulation approaches, significant gaps remain in understanding the mechanical behavior, microstructural evolution, and void coalescence mechanisms in Fe-Cr-Ni alloys with twin boundaries under multiaxial tensile deformation (uniaxial, biaxial, and triaxial). This study seeks to bridge these gaps by utilizing MD simulations to explore the mechanical properties, phase transformations, solid volume and surface area, nanoporous radius, and the mechanisms of void growth and coalescence, including their rates, under multiaxial loading conditions. These factors are critical for optimizing design, enhancing performance, and preventing material failure in applications subjected to complex loading conditions. Key analyses include stress–strain behavior, dislocation density evolution, crystal structure transitions, and void characteristics such as average nanopore radius, surface area, and volume. These insights contribute to a comprehensive understanding of the fracture mechanisms of Fe-Cr-Ni alloys under multiaxial deformation, enabling better predictions of their performance and reliability in demanding applications.

2. Molecular Dynamics Simulation

MD simulations (Ref 51, 52) were carried out using the constant number of atoms, volume, and temperature (NVT) ensembles to investigate the multiaxial tensile deformation of Fe-Cr-Ni alloys. The interatomic interactions were modeled using the Finnis–Sinclair (FS) (Ref 53) embedded atom method (EAM) potential parameterized by Zhou et al. (Ref 54). This potential was chosen because it has been extensively validated for Fe-Cr-Ni alloys and effectively captures their structural and mechanical behaviors, including defect formation and evolution. While recent studies (Ref 44) highlight variability in results with different potentials, the FS EAM potential provides an appropriate balance of accuracy and computational efficiency for simulating the alloy's multiaxial deformation. The total interaction potential energy, E, is given by

$$E = \sum_i \varepsilon \left[\frac{1}{2} \sum_{j \neq i} \mathrm{V}(r_{ij}) - c\sqrt{\rho_i} \right] \quad \text{(Eq 1)}$$

$$V(r_{ij}) = \left(\frac{a}{r_{ij}} \right)^n \quad \text{(Eq 2)}$$

$$\rho_i = \sum_{j \neq i} \left(\frac{a}{r_{ij}} \right)^m \quad \text{(Eq 3)}$$

where r_{ij}, a, c, n, m, and ε are the separation between *ith* and *jth* atom, lattice parameter, and other positive constants. $V(r_{ij})$ is the pair intra-atomic potential energy to account for each atom and ρ_i the local charge density. Equation 1-3 can be written in the generalized form of Hamiltonian pertaining to Fe-Cr-Ni alloy atoms as given below

$$H = \frac{1}{2} \left[\sum_{i \neq j} \sum \hat{p}_i \hat{p}_j V(r_{ij}) \right] - d \sum_i \hat{p}_i \left[\sum_{j \neq i} \hat{p}_j \emptyset(r_{ij}) \right]^{1/2} \quad \text{(Eq 4)}$$

$$\widehat{p}_i = \begin{cases} 1, \textit{if site i is occupied by a metal atom}, \\ 0, \textit{if site i is not occupied by a metal atom} \end{cases} \quad \text{(Eq 5)}$$

$$V(r) = \varepsilon \left[\frac{a}{r} \right]^n \quad \text{(Eq 6)}$$

$$\emptyset(r) = \varepsilon \left[\frac{a}{r} \right]^m \quad \text{(Eq 7)}$$

$$d = \varepsilon \times c \quad \text{(Eq 8)}$$

where ø (r) represents the Local electron density distribution function and d is defined as the product of the constants ε and c representing a scaled interaction parameter. The Newtonian equation of motion of an atom, *i,* of mass (*w*), due to the both inter- and intra-atomic forces arising from various potentials can be written as

$$w \times \frac{d^2 \boldsymbol{r}_i}{dt^2} = \boldsymbol{F}_i = -\nabla_i E \quad \text{(Eq 9)}$$

where $\boldsymbol{F}_i$ represent the total force acting on the *i*th atom. The Eq 9 is solved by velocity Verlet algorithm (Ref 47) with a time step (Δt) of 1 femto-second as given in equations number (10)-(11)

$$\boldsymbol{r}_i(t + \Delta t) = \boldsymbol{r}_i(t) + \boldsymbol{v}_i(t)\Delta t + \frac{1}{2}(\Delta t)^2 \boldsymbol{a}_i(t + \Delta t) \quad \text{(Eq 10)}$$

$$\boldsymbol{v}_i(t + \Delta t) = \boldsymbol{v}_i(t) + \frac{1}{2}\Delta t[\boldsymbol{a}_i(t) + \boldsymbol{a}_i(t + \Delta t)] \quad \text{(Eq 11)}$$

Here, $\boldsymbol{v}_i$ and $\boldsymbol{a}_i$ and are the velocity and acceleration of the *i*th atom. The Nose–Hoover thermostat (Ref 55, 56) has been used to control the variation in temperature of the simulation system. Multiaxial tensile compressive deformation at a constant strain rate has been applied to the system. The elements of the tensor of stresses (Ref 57) were calculated as

$$\sigma_{\alpha\beta}(i) = -\frac{1}{\Omega_0} \left[\frac{1}{2} \sum_j F_{ij}^{\alpha} r_{ij}^{\beta} + M_i v_i^{\alpha} v_i^{\beta} \right] \quad \text{(Eq 12)}$$

where α and β denote the Cartesian components, F_{ij} is the force on atom i due to another atom j, Ω_0 is the volume. M_i is the mass of atom i, and v_i is the velocity of atom i. The multiaxial deformation of system is carried out at fixed temperature at a fixed strain rate, *i.e.*, $10^9 s^{-1}$. Molecular dynamics simulations are carried out by Large-Scale Atomic/Molecular Massively Parallel Simulator (LAMMPS) an open-source software. Visualization and analysis of simulation data have been carried out by Open Visualization Tool (Ref 58) software packages. The data analysis was performed using the Open Visualization Tool (OVITO) software (Ref 59, 60). The adaptive common neighbor analysis (aCNA) method (Ref 61) was employed to evaluate the local crystallinity of atoms inside a Fe-Cr-Ni alloy-constructed model. This technique gives different colors to

atoms based on their crystalline environments: FCC, HCP, BCC, and others, which represent green, red, blue, and white, respectively. Moreover, we have applied the DXA method (Ref 62, 63) to examine how dislocations contribute to the behavior of materials under multiaxial tensile deformation. Different types of dislocations form during deformation, along with the initiation of nanovoids.

The ATOMSK software (Ref 64) was used to construct a 3D cubic FCC crystal structure box (112Å × 112Å × 112Å, containing 116,100 atoms) for the Fe-Cr-Ni model, with twin boundaries shown in incorporating HCP crystal structures at twin boundaries along the orientations (1 1 -2), (1 1 1), and (-1 1 0), as shown in Fig. 1. This figure shows (a) atom distribution, (b) % composition of element in Fe-Cr-Ni alloy, (c) constructed model configuration with twin boundary and multiaxial tensile deformation of Fe-Cr-Ni alloy system carried out as (d) uniaxial, (e) biaxial, and (f) triaxial. For uniaxial tensile deformation, straining is carried out along both y direction and other two directions are kept to fixed. For biaxial tensile deformation, straining is carried out along both x and y directions and z direction is kept fixed. For triaxial tensile deformation, straining is carried out along all three directions.

3. Results and Discussion

3.1 Twin Induce Nanovoids Evolution

In this section, we have discussed the nucleation, growth, and coalescence of nanovoids in the layered structure of Fe-Cr-Ni alloys during multiaxial (uniaxial, biaxial, and triaxial) tensile deformation. Figure 2(a)-(c) shows the evolution of crystalline structures and nanovoids during the triaxial tensile deformation. Early stage of triaxial tensile deformation, the Fe-Cr-Ni alloys start to deform, leading to the nucleation of nanovoids. As the deformation continues, these nanovoids grow in size, eventually causing material failure. Additionally, minor amount of meta-stable BCC crystalline structures appears around the void surfaces, due to the gradual local expansion of FCC structures. Triaxial tensile deformation facilitates the crystalline structural transformation in step-wise manner, i.e., FCC to BCC (meta-stable) to random. Our observations pertaining to evolution of meta-stable BCC structures are consistent with Ostwald step rule. According to this rule, the solid phase first transformed into the least stable structure or meta-stable, before random or liquid phase. Figure 2(c) shows the nucleation of voids at a strain of 0.106, which appear as mesh defects. As deformation progresses, these voids grow in size under tensile stress, eventually leading to fracture initiation and propagation, resulting in material failure (Ref 65, 66). Furthermore, multiple dislocations arise along the surface of the mesh defects, as seen in the figure. The yellow color mesh denotes the voids mess defect. Moreover, for the clear

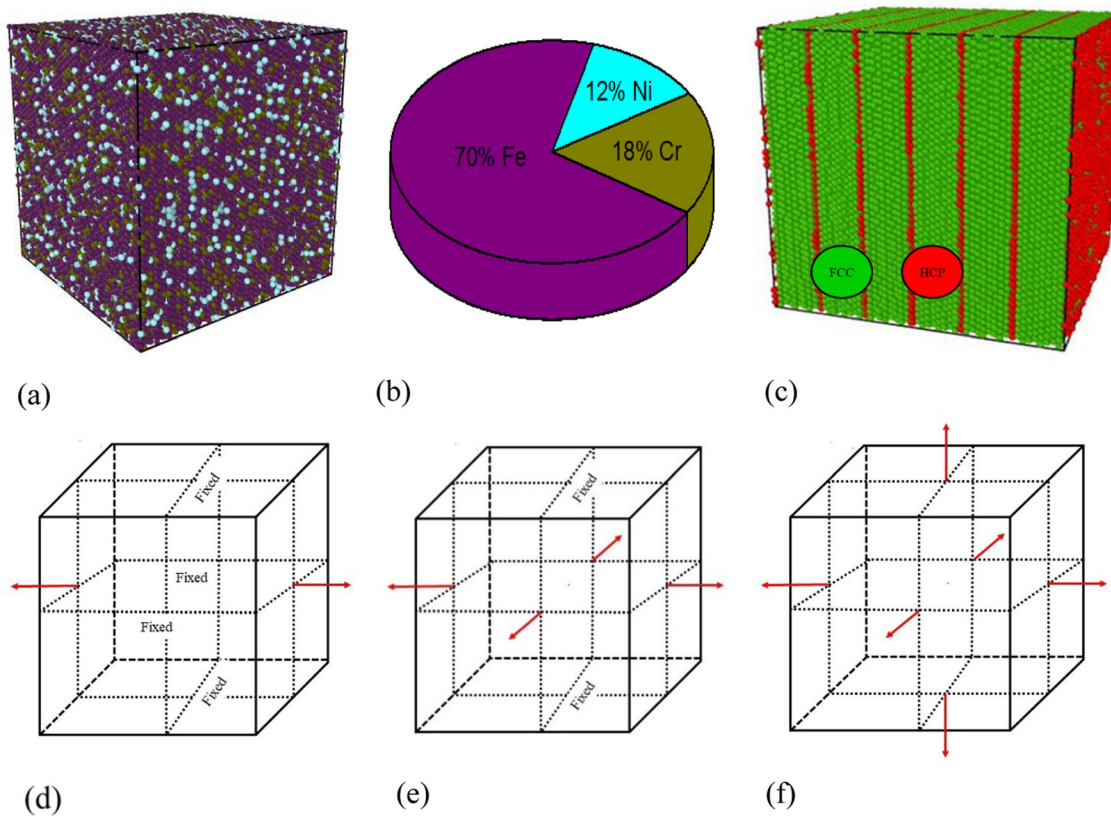

Fig. 1 Snapshots of Fe-Cr-Ni alloys constructed model with a multiaxial (uniaxial, biaxial and triaxial) tensile deformation: (a) atomic distribution, (b) composition, (c) layered structure, (d) uniaxial tensile deformation, (e) biaxial tensile deformation, (f) triaxial tensile deformations (Color figure online)

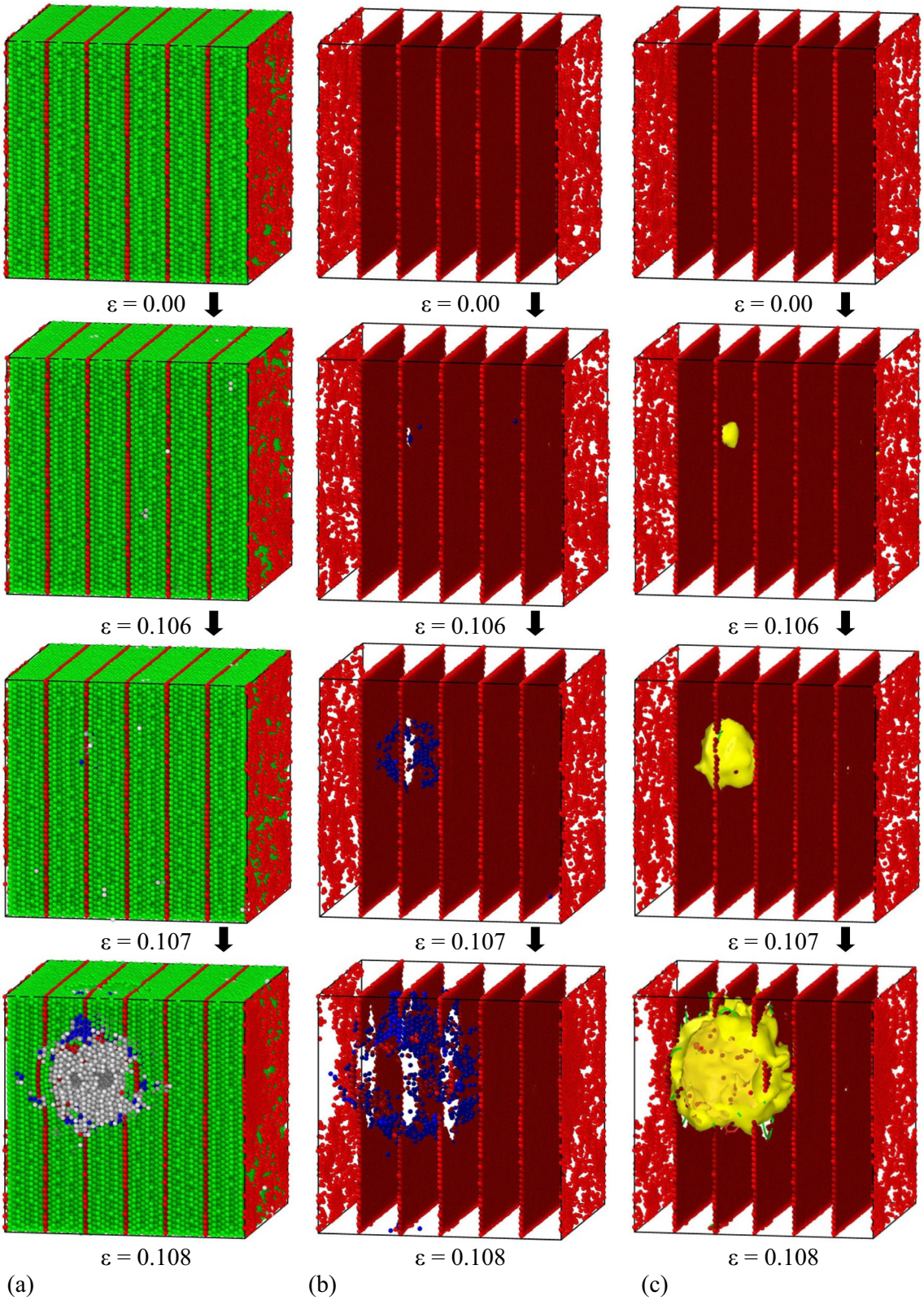

Fig. 2 Triaxial tensile deformation of Fe-Cr-Ni alloys with twin boundaries: (a) initial configuration of atom block, (b) configuration after deletion of FCC and other atoms, (c) formation of mess defect with various dislocation. The green, red, blue, and white atoms represent FCC, HCP, BCC, and amorphous structures, respectively. Additionally, the yellow colors denote mesh defects (Color figure online)

visualization, we have created side views of simulation system as shown in Fig. 3.

Figure 4 shows the formation and evolution of voids in an Fe-Cr-Ni alloy with twin boundaries, shown alongside the stress–strain curve during triaxial tensile deformation driven by

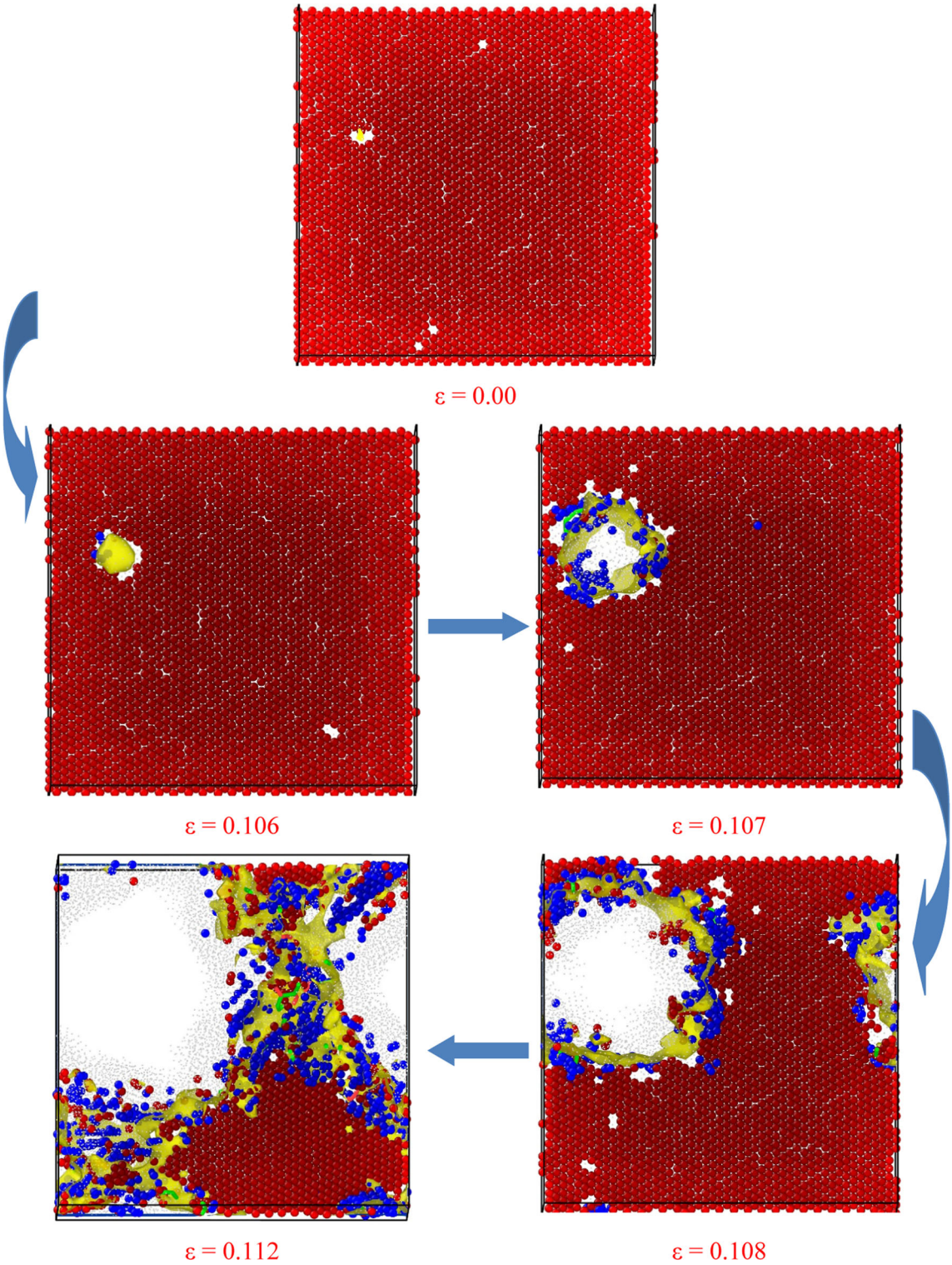

Fig. 3 Development of microvoid cavity in Fe-Cr-Ni alloy with twin boundary during tiaxial tensile deformation. Red, blue, and white spherical atom represent HCP, BCC, and amorphous structure atom, respectively. Yellow indicates mesh defects, while green and red lines represent Shockley and other type dislocations (Color figure online)

strain-induced phase transformation. Void nucleation begins beyond the yield point, where significant lattice stretching occurs, preventing void formation in the elastic region. As tensile deformation progresses, voids nucleate along twin boundaries, subsequently growing and coalescing, which critically contributes to the ductile fracture process. After yielding, a transient stress value of approximately -5 GPa is observed, due to the sudden large-scale slipping during deformation. As deformation continues, the growth and merging of voids significantly reduce the material's load-bearing capacity, leading to a drop in apparent stress. The final fracture is characterized by the formation of a semi spherical cavity due

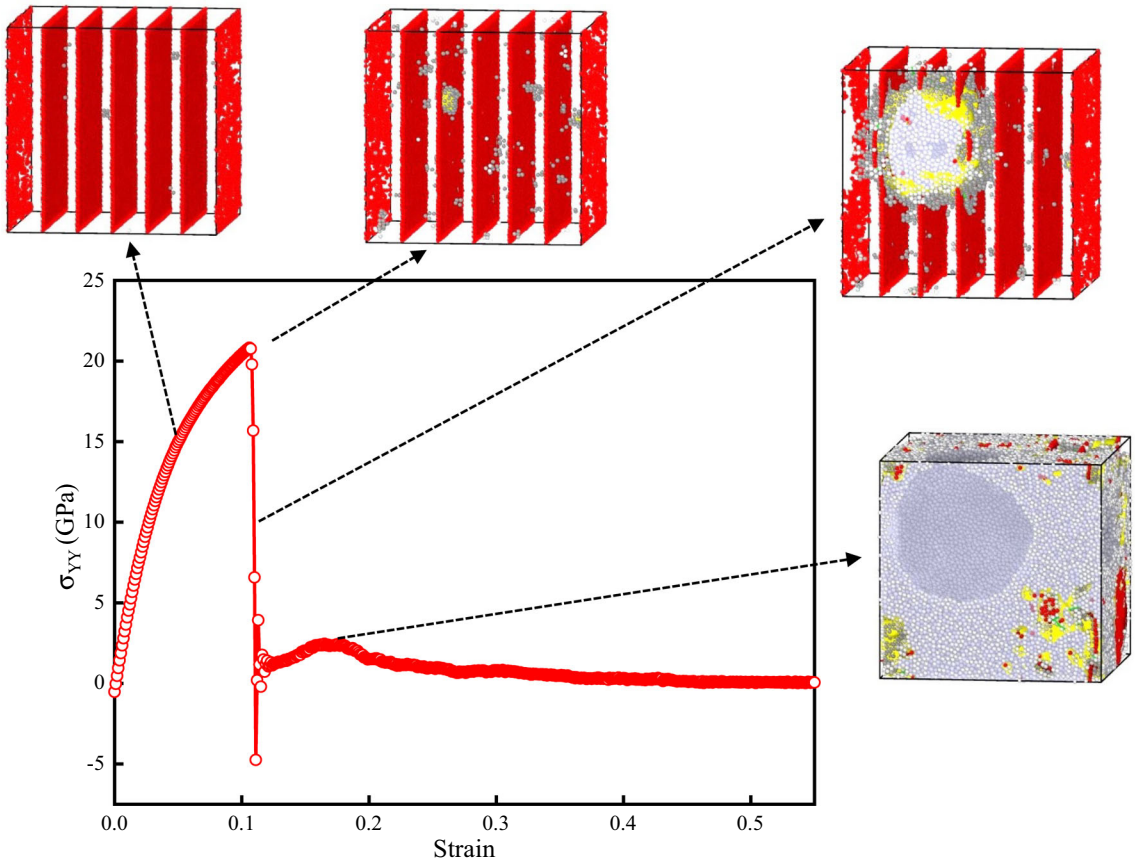

Fig. 4 Gradual growth of voids view after deleting FCC atom along stress–strain plots during triaxial tensile deformation of Fe-Cr-Ni alloys with twin boundaries where red, white, and yellow colors represent HCP, others atoms and mess defect, respectively

to isotropic void growth under hydrostatic stress and the coalescence of adjacent voids.

Several researchers have reported similar phenomena in experimental studies on alloys subjected to tensile deformation, particularly concerning the role of pre-existing twins. For instance, Hong et al. (Ref 67) investigated the effect of pre-existing twinning on strain localization in Mg alloys during in situ tensile deformation. They observed strain concentration at grain and twin boundaries due to inefficient plastic strain transfer mechanisms, demonstrating the critical role of twin boundaries in governing deformation behavior. Similarly, Zhang et al. (Ref 68) examined the impact of pre-existing twins on the mechanical properties and microstructural evolution of AZ31 Mg alloys during uniaxial compression. Their study revealed that twins influenced dynamic recrystallization and mechanical properties, akin to the nanoscale mechanisms involving twins discussed in our study. Additionally, Xue et al. (Ref 69) explored pre-existing twins in Laves phase V_2Hf alloys and their interaction with dislocations. Their findings demonstrated that twins facilitated twin growth during compression, leading to reduced compressive strength and plastic strain. These observations align with the deformation characteristics identified in our simulations. Figure 5 shows variation in the dislocation density with strain when there is an Fe-Cr-Ni alloy with twin boundaries during triaxial tensile deformation. Initially, within the elastic region, no dislocations are appeared. However, at the yield point, there is a peak in dislocation density. Dislocations, including Shockley partials and perfect dislocations, act as obstacles to the atoms at the twin boundary cracking surfaces. The blue arrows indicate the Burgers vector, which is perpendicular to the dislocation line. The green and red lines represent Shockley partial and perfect dislocations, respectively. Furthermore, we have estimated percentage of several types of crystalline structure transformation including HCP, BCC, FCC, ICO, and other structure during triaxial tensile deformation of Fe-Cr-Ni alloys with twin boundary as shown in Fig. 6. We have observed that, beyond the yield point ($\varepsilon > 0.106$), the initial FCC and HCP structures begin to transform into BCC, ICO, and other crystalline structure. When the strain value ($\varepsilon = 0.15$) exceeds, most of the atoms in Fe-Cr-Ni alloy atoms transition into a random arrangement. This transformation leads to final state characterized by a disordered structure, commonly known as an amorphous structure, due to coalescence and growth of nanovoids. During the triaxial tensile deformation of a Fe-Cr-Ni alloy with twin boundaries, we observed variations in total energy (TE), surface area (S), solid volume (V_{solid}), and radius of nanovoids (R_{void}). Initially, in the elastic region ($\varepsilon \leq 0.106$), the TE and V_{solid} plots show continuous rise, and no nanovoids are formed. Beyond the yield point ($\varepsilon \geq 0.106$), the TE and S gradually increase. This is due to the rise in internal energy as the Fe-Cr-Ni alloy undergoes plastic deformation, leading to the nucleation and growth of voids. Meanwhile, V_{solid} decreases because the formation and growth of nanovoids reduce the overall density of the solid material, as shown in Fig. 7.

Additionally, we have investigated the evolution of crystal structure changes and defect formation in an Fe-Cr-Ni alloy with a twin boundary during biaxial tensile deformation, as

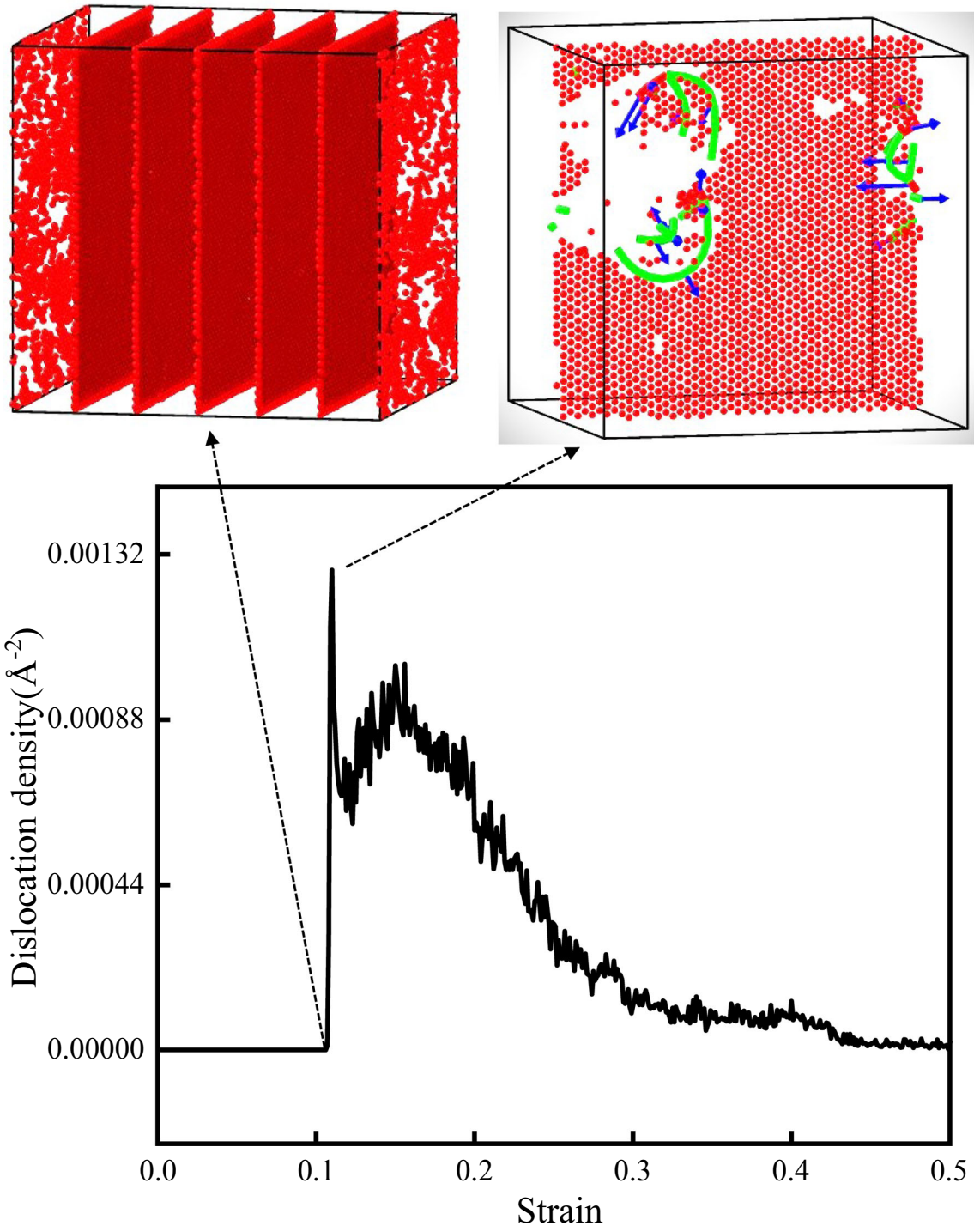

Fig. 5 Role of dislocation in the dislocation density vs strain plots. The green and red line represents Shockley and other type of dislocations, respectively, with their Burger vectors and slip systems identified as 1/6[-1 -2 -1], (111) [-1 -2 -1] for Shockley dislocations and 1/18[11 -7 -8], (1 1 1) [11 -7 -8] for other type of dislocations. The blue arrow indicates the Burger vectors scale by a factor 6 for visualization

shown in Fig. 8(a) and (b). We have observed that the Fe-Cr-Ni alloy with a twin boundary deforms and nucleates defects and voids earlier as compared to triaxial deformation. At a strain value of 0.104, intrinsic and extrinsic stacking faults are formed, while in Fig. 8(b), the defective internal structure is displayed after removing the perfect FCC and other structure atoms. The colors of the atoms indicate yellow represents mess defects, green signifies Shockley partial dislocations, and red denotes stacking faults. Similarly, Fig. 9 shows the impact of uniaxial tensile deformation on the crystal structure of the Fe-Cr-Ni alloy with twin boundaries. It was noted that the Fe-Cr-Ni alloy begins to deform earlier under uniaxial tension compared to biaxial and triaxial tensile deformation. The defective structure after the FCC and other structural atoms have been removed, revealing various dislocations and defects. Under applied stress, dislocations move along specific slip

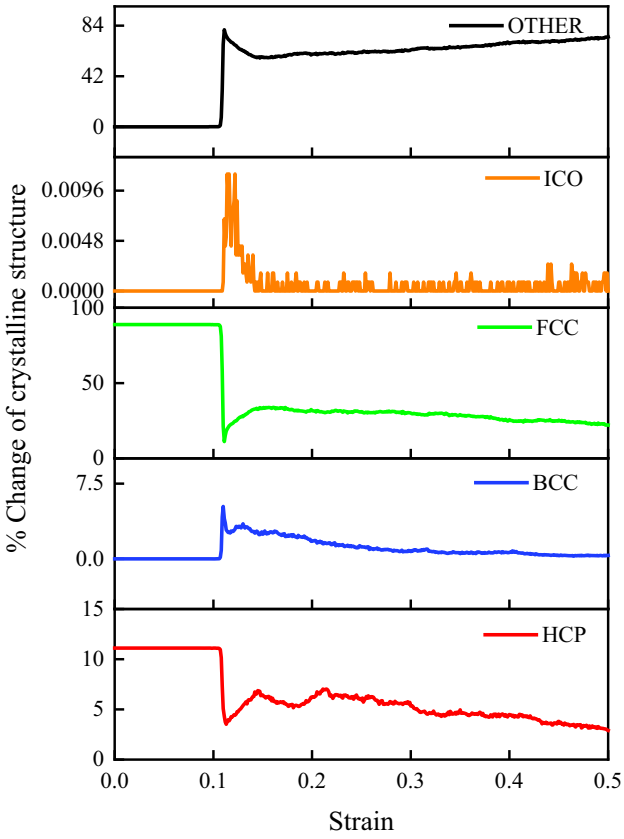

Fig. 6 Percentages change of crystalline structure of HCP, BCC, FCC, ICO, and other crystalline atoms in Fe-Cr-Ni alloy with twin during triaxial tensile deformation at an applied strain rate of 10^9 S^{-1} at 300K

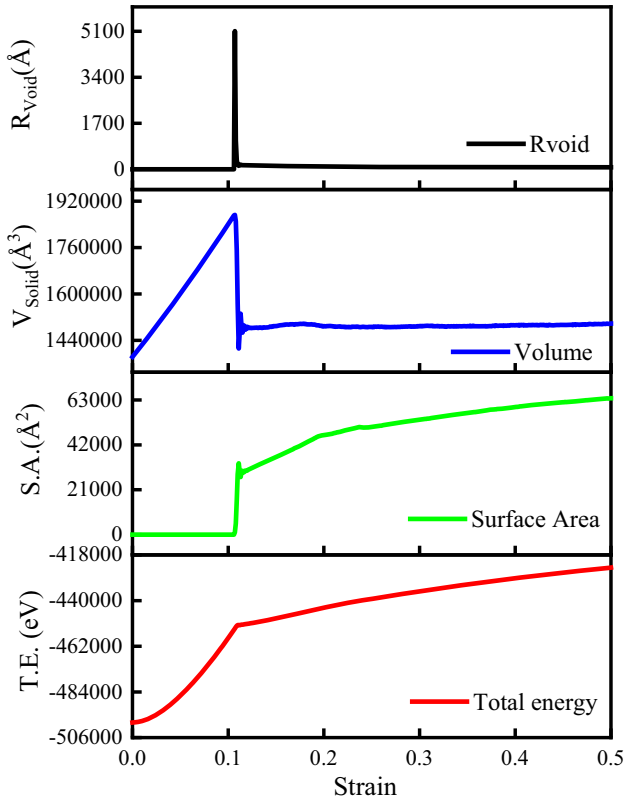

Fig. 7 Variation in total energy, surface area, solid volume, and nanovoid radius in Fe-Cr-Ni alloy with twin boundary during triaxial tensile deformation

systems and interact with stacking faults. The dynamic behavior of these dislocations under stress leads to complex interactions and the formation of dislocation tangles. These dislocation tangles play a crucial role in the hardening process of the Fe-Cr-Ni alloy. The green, blue, pink and red line represents Shockley, perfect, stair rod, and other types of dislocations, respectively. Burger vectors and slip systems are identified as 1/6[2 1 -1], (11-2) [1 1 -1] for Shockley dislocations, 1/2[0 1 1], (1 1 -2) [0 1 1] for perfect dislocation, 1/6[0 -1 -1], (1 1 -2) [0 -1 -1] for stair rod dislocation, and 1/18[-5 -5 2], (1 1 -2) [-5 -5 2] for other type of dislocations.

3.2 Nanovoid Evolution in the Absence of Twin

The study of crystal structure phase transformations of Fe-Cr-Ni alloys without twin boundaries under multiaxial tensile deformations (uniaxial, biaxial, and triaxial) reveals notable differences in behavior and microstructural evolution. As shown in Fig. 10(a), (b), and (c), the material demonstrates distinct phase transformation mechanisms based on the loading direction applied. Under uniaxial tensile deformation, the Fe-Cr-Ni alloys initially exhibit a transformation from the FCC phase to a meta-stable BCC phase due to lattice distortion. As deformation progresses, this phase evolves into a complex network of multiple stacking faults involving FCC, HCP, and twin nucleation within rectangular grain boundaries. Continued deformation results in the formation of alternating layers of HCP and FCC atoms within rhombus-shaped grain boundaries, indicating further structural instability. The presence of amorphous atoms along these boundaries suggests significant atomic disorder, which often precedes void nucleation and eventual material failure, as shown in Fig. 10(a). In biaxial tensile deformation, the transformation from FCC to BCC is less pronounced compared to uniaxial deformation due to greater stress constraints. Further deformation creates complex stacking fault structures with rectangular and square shapes. Continued deformation at the intersections of these stacking faults leads to the formation of nanovoids filled with amorphous atoms, contributing to material failure as shown in Fig. 10(b). During triaxial tensile deformation, FCC atoms transform into amorphous structures more readily. As deformation continues, multiple voids nucleate, surrounded by BCC atoms. The coalescence of these microvoids ultimately leads to material failure as shown in Fig. 10(c). Notably, the Fe-Cr-Ni alloy fails more quickly under triaxial deformation compared to biaxial and uniaxial conditions. These observations highlight the alloy's sensitivity to the type of applied stress, with varying degrees of phase transformation, stacking fault formation, and material failure dependent on the deformation mode.

3.3 Comparative Analysis of Rupture Mechanisms with and Without Twin

The stress–strain response plots of Fe-Cr-Ni alloys with containing multiple twin boundary during multiaxial tensile deformation are shown in Fig. 11(a), (b), (c), and (d). We observed that triaxial tensile deformation shows highest yield stress compared to the bi- and uniaxial tensile deformations.

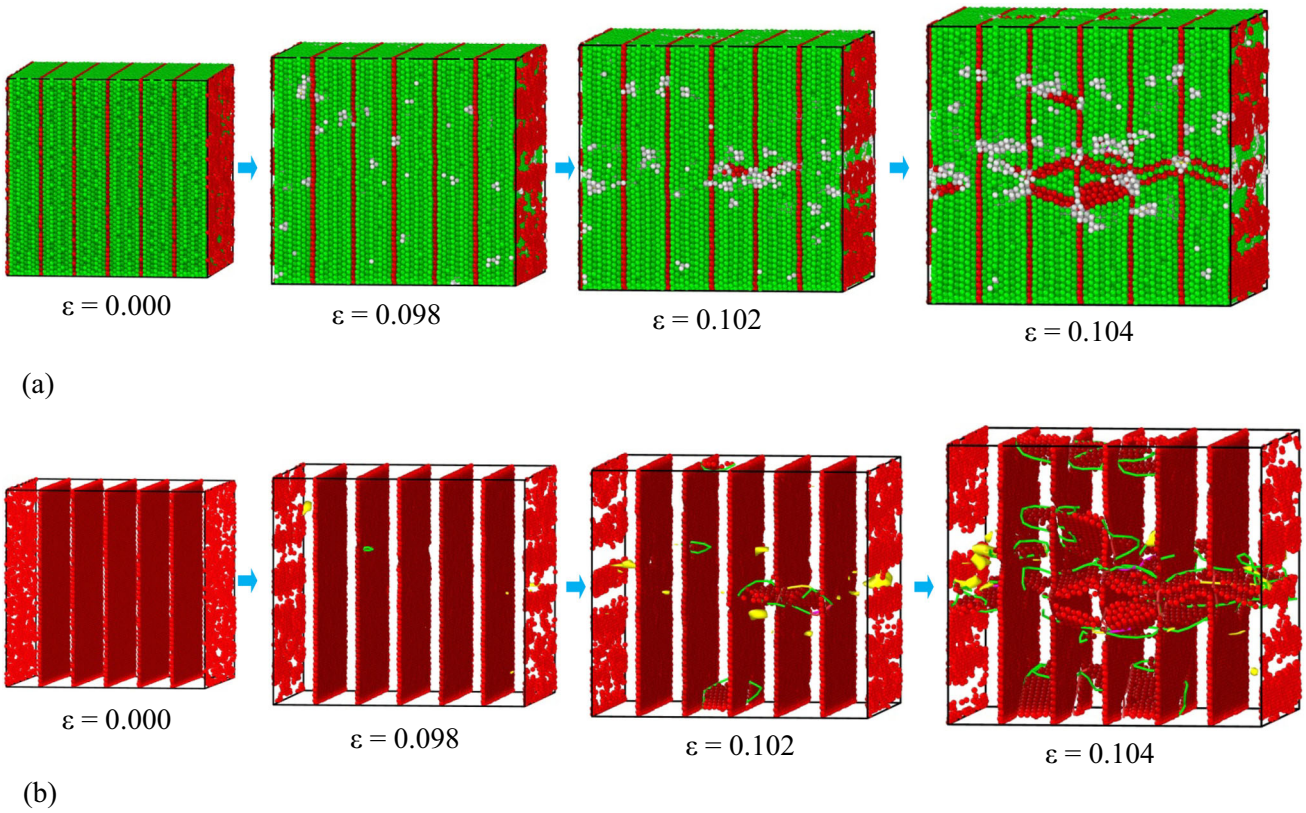

Fig. 8 Biaxial tensile deformation of Fe-Cr-Ni alloys with twin boundaries: (a) changes in crystal structure phases, (b) formation of defects: mess defect, stacking faults, and various dislocations shown by snapshots after deleting FCC and other atoms

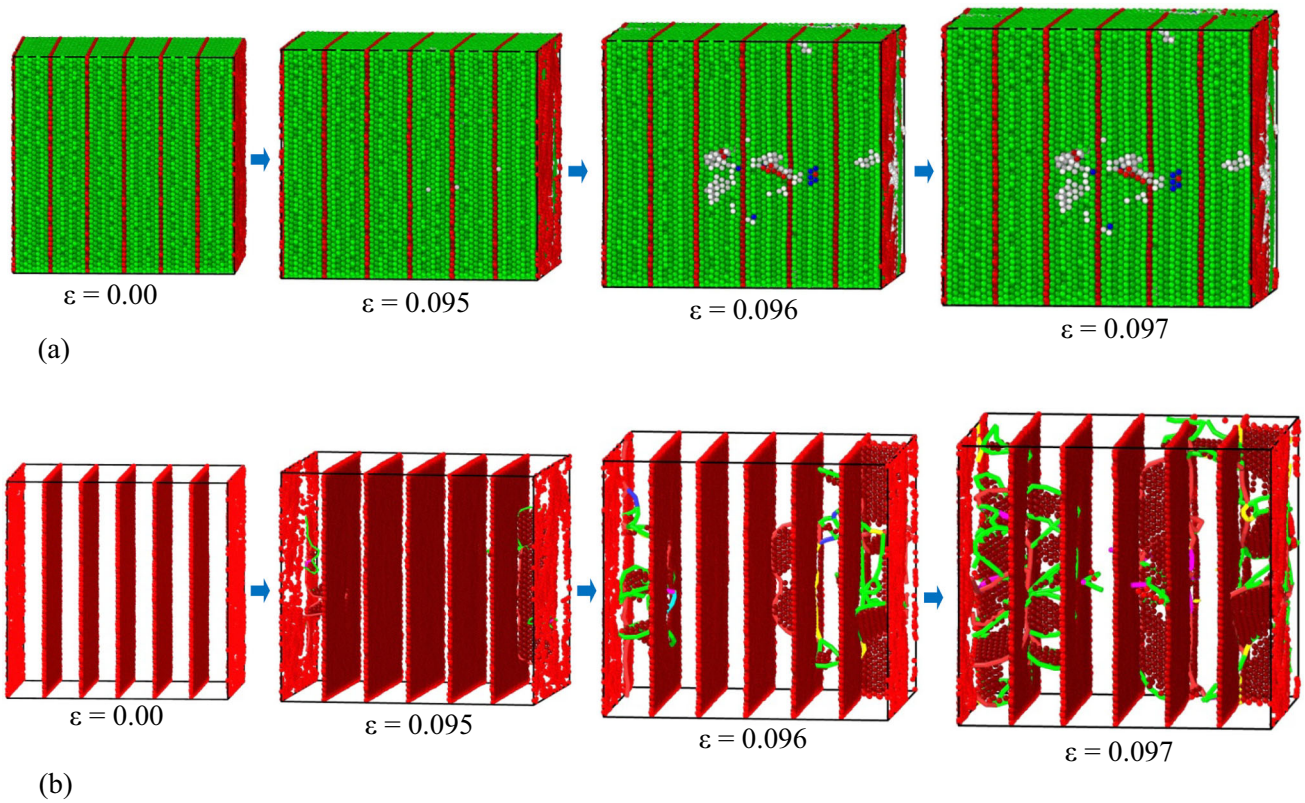

Fig. 9 Uniaxial tensile deformation of Fe-Cr-Ni alloys with twin boundaries: (a) changes in crystal structure phases, (b) formation of stacking faults and various dislocations

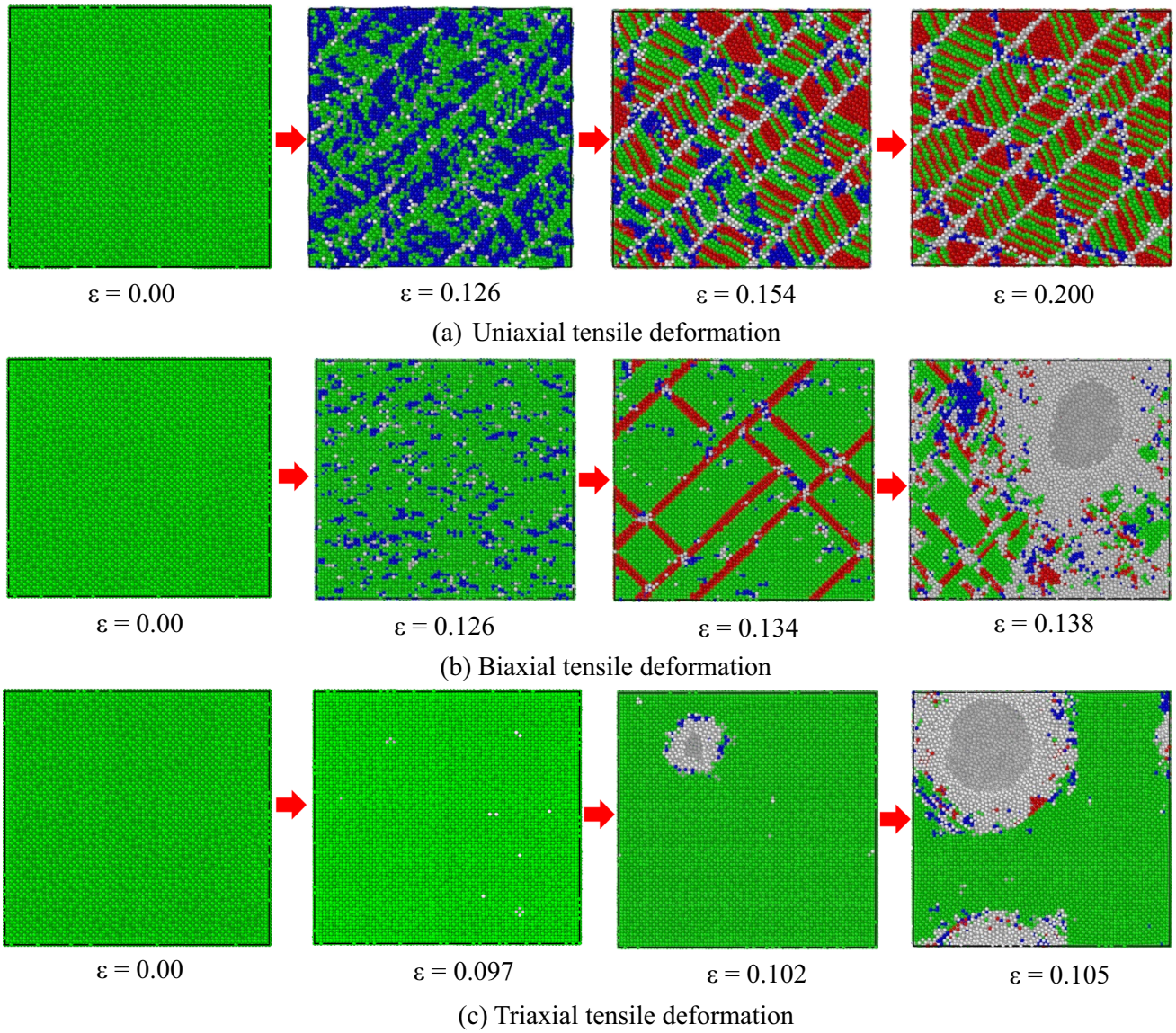

Fig. 10 Snapshot of tensile deformation of Fe-Cr-Ni alloy without twin boundaries during multiaxial deformation, (a) uniaxial, (b) biaxial, (c) triaxial at various strain values. Green, red, blue, and white atom represents the FCC, HCP, BCC, and other atoms

This occurs due to different constraints and stress distributions in each deformation mode, which influence material behavior and result in changes in yield stress and the size of the elastic zone. Moreover, we can see in Fig. 11(b) their dislocation vs. strain plots. During uniaxial, biaxial, and triaxial tensile deformation, dislocation density peaks at the yield point decrease and then slightly increase before gradually declining. Initially, dislocations rapidly multiply and interact, leading to some annihilation. Continued deformation generates new dislocations or activates immobile ones, causing a secondary density increase. Eventually, dislocations rearrange into stable structures like sub-grains, reducing overall dislocation density as they become less mobile. Furthermore, Fig. 11(c) presents the stress–strain curves of Fe-Cr-Ni alloys without twin boundaries. The results indicate a slight decrease in yield stress but an increase in the breaking point during triaxial, biaxial, and uniaxial tensile deformation, respectively. This can be attributed to the fact that in triaxial and biaxial stress states, the material is more constrained, leading to more uniform plastic deformation. Conversely, uniaxial deformation reduces the localization of deformation and limits the development of strain hardening. Figure 11(d) shows the dislocation density versus strain plots for Fe-Cr-Ni alloys without twin boundaries. The results show that at the yield point during triaxial, biaxial, and uniaxial deformation, the dislocation density increases; however, a slight decrease in dislocation density is observed in uniaxial, biaxial, and triaxial tensile deformation, respectively.

For the quantitative characterization of crack formation and material failure under multiaxial loading conditions, we have shown plots of changes in mess surface area and solid volume with variation in strain in Fe-Cr-Ni alloy with and without containing twin boundaries. In Fig. 12(a) and (b), the changes in surface area (SA) and solid volume of Fe-Cr-Ni alloys with twin boundaries are shown during uniaxial, biaxial, and triaxial tensile deformation. The SA remains zero during the proportional limit of the stress–strain response of the Fe-Cr-Ni alloy with twin boundaries. In the early stages of plastic deformation, SA increases during triaxial and biaxial tensile deformation, but

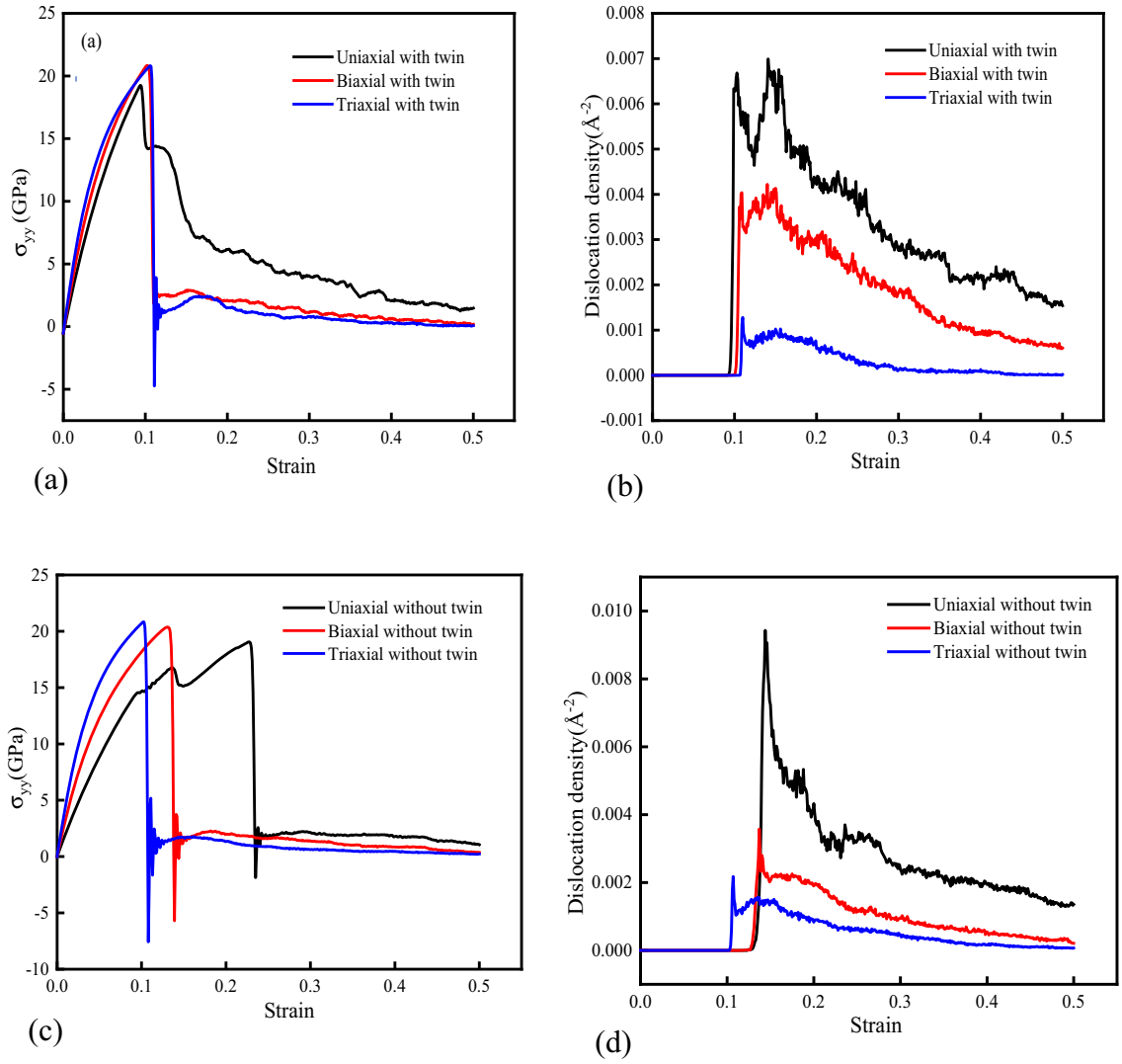

Fig. 11 Stress–strain response and dislocation density–strain plots of Fe-Cr-Ni alloys with twin boundary (a, b) and without twin boundary (c, d) during multiaxial tensile deformation

remains nearly zero during uniaxial deformation. In the plastic region, SA continuously increases, driven by the nucleation of multiple voids, with the most significant increase occurring during triaxial tensile deformation due to the complex stress state, as shown in Fig. 12(a). In Fig. 12(b), the changes of solid volume increase linearly in the elastic region due to the increased separation between nearest neighbor atoms in the Fe-Cr-Ni alloys. Beyond the yield point, the solid volume decreases as a result of nanovoid nucleation. After the nucleation of nanovoids, the Fe-Cr-Ni alloys with twin boundaries contract, and the atoms eventually settle into their natural nearest neighbor positions. Furthermore, for knowing the influence of twin boundary effect inside the Fe-Cr-Ni alloy during multiaxial tensile deformation, we have also investigated the variation in surface area and changes of solid volume with variation in strain in Fe-Cr-Ni alloy without twin boundary. Figure 12(c) and (d) shows the variation in SA and solid volume with variation in strain plots. The changes of SA are nearly zero before the yield point, but at yield point the SA is constantly increasing. After the yield point, the SA decreases and then continuously increases with the increase in strain in order to triaxial, biaxial, and uniaxial tensile deformation, respectively, due to formation nanovoids shown in Fig. 12(c). The changes of solid volume are linearly increasing up to yield point due to the increased separation between nearest neighbor atoms in the Fe-Cr-Ni alloys. After yield point, it is slightly decreasing due to creation of nanovoids as shown in Fig. 12(d).

4. Conclusion

The aim of this study systematically examined the impact of twin boundaries on the formation, growth, and coalescence of nanovoids in Fe-Cr-Ni alloys under multiaxial tensile deformation. The following are the main conclusions drawn from the simulations:

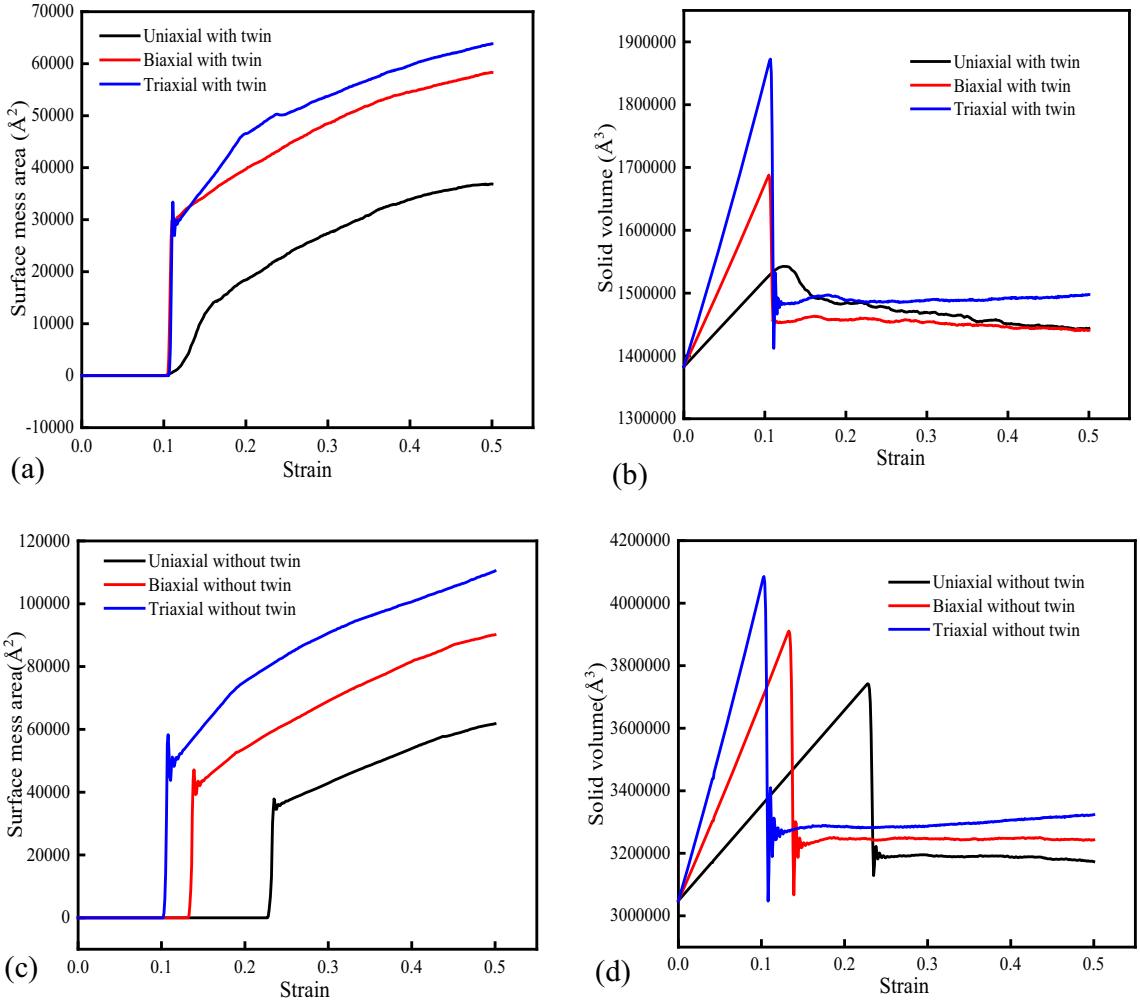

Fig. 12 Variation in surface mess area and solid volume in Fe-Cr-Ni alloys model with twin boundary (a, b) and without twin boundary (c, d) during multiaxial tensile deformation

1. The presence of twin boundaries significantly accelerates nanovoid nucleation and growth in Fe-Cr-Ni alloys during triaxial tensile deformation, leading to rapid material failure. The BCC phase transformations predominantly occur around void surfaces, driven by strain-induced mechanisms near twin boundaries.
2. Triaxial tensile deformation in Fe-Cr-Ni alloys with twin boundaries produces no dislocations initially, but dislocation density peaks at the yield point; while strain increases, the structures transform from FCC and HCP to BCC, ICO, and amorphous.
3. When comparing the yield stress and the narrowing of the elastic zone in Fe-Cr-Ni alloys with twin boundaries during uniaxial, biaxial, and triaxial deformations, the triaxial deformation has a significant influence.
4. Fe-Cr-Ni alloys without twin boundaries exhibit unique stacking fault forms and void nucleation patterns that are linked to material failure, depending on the type of multiaxial tensile deformation causing the crystal structure phase changes.

The presence of twin boundaries in Fe-Cr-Ni alloys plays a crucial role in their mechanical behavior under multiaxial tensile deformation, reducing dislocation mobility, restricting surface area expansion, and minimizing changes in solid volume, whereas Fe-Cr-Ni alloys without twin boundaries show more significant surface area expansion in the plastic region and greater solid volume increase in the elastic region, driven by enhanced void nucleation and growth. These results reveal that yield stress, surface area changes, and elastic–plastic behavior during multiaxial tensile deformation are significantly impacted by twin boundaries in Fe-Cr-Ni alloys.

Data Availability

Data supporting this study's findings are available from the corresponding author upon reasonable request.

Conflict of interest

The authors declare no conflict of interest regarding this publication.

References

1. G. Geogy, and H. Shaikh, *Introduction to austenitic stainless steels*, Corrosion of Austenitic Stainless Steels, Elsevier, 2002

2. A.A. Lebedev, and V.V. Kosarchuk, Influence of Phase Transformations on the Mechanical Properties of Austenitic Stainless Steels, *Int. J. Plast.*, 2000, **16**, p 749–767
3. P. Behjati, A. Kermanpur, A. Najafizadeh, and H.S. Baghbadorani, Microstructural Investigation on Deformation Behavior of High Purity Fe–Cr–Ni Austenitic Alloys during Tensile Testing at Different Temperatures, *Mater. Sci. Eng.: A*, 2014, **618**, p 16–21
4. Y.Z. Xia, H. Bei, Y.F. Gao, D. Catoor, and E.P. George, Synthesis, Characterization, and Nanoindentation Response of Single Crystal Fe–Cr–Ni Alloys with FCC and BCC Structures, *Mater. Sci. Eng.: A*, 2014, **611**, p 177–187
5. M.M. Mourad, H.A. Saudi, M.M. Eissa, and M.Y. Hassaan, Modified Austenitic Stainless-Steel Alloys for Shielding Nuclear Reactors, *Prog. Nucl. Ener.*, 2021, **142**, p 104009
6. R.K. Desu, H.N. Krishnamurthy, A. Balu, A.K. Gupta, and S.K. Singh, Mechanical Properties of Austenitic Stainless Steel 304 and 316L at Elevated Temperatures, *J. Mater. Res. Tech.*, 2016, **5**, p 13–20
7. C. Zhang, C. Wang, S.L. Zhang, Y.L. Ding, Q.L. Ge, and J. Su, Effect of Aging Temperature on the Precipitation Behavior and Mechanical Properties of Fe–Cr–Ni Maraging Stainless Steel, *Mater. Sci. Eng.: A*, 2021, **806**, p 140763
8. I. Toor, P.J. Hyun, and H.S. Kwon, Development of High Mn–N Duplex Stainless Steel for Automobile Structural Components, *Corro. Sci.*, 2008, **50**, p 404–410
9. A.S. Podder and A. Bhanja, Applications of Stainless Steel in Automobile Industry, *Adv. Mater. Res.*, 2013, **794**, p 731–740
10. A. Kumar, R. Kumar, S. Kumar, and A. Kumar, Atomistic Structural Transformation of Fe-Cr-Ni Single Crystal Alloy under Uniaxial Deformation using Molecular Dynamics Simulation, *Mater. Tod.: Proceed.*, 2023 https://doi.org/10.1016/j.matpr.2023.09.045
11. A. Kumar, S. Kumar, and A. Kumar, Structural Phase Transformation in Single-Crystal Fe–Cr–Ni Alloy During Creep Deformation Using Molecular Dynamics Simulation and Regression-Based Machine Learning Methodology, *Bullet. Mater. Sci.*, 2024, **47**, p 1–11
12. R.R. Kumar, R.K. Gupta, M. Sadhasivam, K.G. Pradeep, and M.J.N.V. Prasad, Mechanical Behaviour and Interface Correlative Microscopic Analysis of Vacuum Diffusion Bonded Dissimilar Stainless Steel/α-Ti Alloy Joint for Aerospace Applications, *Vacuu.*, 2023, **217**, p 112561
13. J. Li, D. Zhan, Z. Jiang, H. Zhang, Y. Yang, and Y. Zhang, Progress on Improving Strength-Toughness of Ultra-High Strength Martensitic Steels for Aerospace Applications: A Review, *J. Mater. Res. Tech.*, 2023, **23**, p 172–190
14. C.C. Silva, H.C. Miranda, H.B. de Sant'Ana, and J.P. Farias, Austenitic and Ferritic Stainless Steel Dissimilar Weld Metal Evaluation for the Applications As-Coating in the Petroleum Processing Equipment, *Mater. Des.*, 2013, **47**, p 1–8
15. H.M. Tawancy, Failure Analysis of 304 Stainless Steel Components Used in Petrochemical Industry Applications, *Metall., Microst Analy.*, 2019, **8**, p 705–712
16. K.L. Cashell, and N.R. Baddoo, Ferritic Stainless Steels in Structural Applications, *Thin-Wall. Struct.*, 2014, **83**, p 169–181
17. L. Gardner, A. Talja, and N.R. Baddoo, Structural Design of High-Strength Austenitic Stainless Steel, *Thin-wall. Struct.*, 2006, **44**, p 517–528
18. H.J. Cho, S.H. Kim, Y. Cho, and S.J. Kim, Effect of Copper Addition on Tensile Behavior in Fe-Cr-Ni Stable Austenitic Stainless Steel, *Mater. Charact.*, 2022, **190**, p 112052
19. A.M. Bandar, R. Mongrain, E. Irissou, and S. Yue, Improving the Strength and Corrosion Resistance of 316L Stainless Steel for Biomedical Applications using Cold Spray, *Surf. Coat. Techn.*, 2013, **15**(216), p 297–307
20. Y. Li, C. Ma, F. Qin, H. Chen, X. Zhao, R. Liu, and S. Gao, The Microstructure and Mechanical Properties of 316L Austenitic Stainless Steel Prepared by Forge and Laser Melting Deposition, *Mater. Sci. Eng.: A*, 2023, **12**(870), p 144820
21. A.K. Mahata, and M.B. Kivy, Computational Study of Nanoscale Mechanical Properties of Fe–Cr–Ni Alloy, *Mole. Simul.*, 2022, **48**(7), p 551–567
22. T. Shu-ping, W.A.N.G. Zhen-Hau, S. Cheng, Z. Liu, J. Han, and W. Fu, Effect of Cu Content on Aging Precipitation Behaviors of Cu-Rich Phase in Fe-Cr-Ni Alloy, *J. Iron Steel Res. Int.*, 2010, **17**(5), p 63–68
23. P. Ou, H. Xing, X.L. Wang, and J. Sun, Tensile Yield Behavior and Precipitation Strengthening Mechanism in Super 304H Steel, *Mater. Sci. Eng.: A*, 2014, **600**, p 171–175
24. A.J. Cao, Y.G. Wei, and S.X. Mao, Deformation Mechanisms of Face-Centered-Cubic Metal Nanowires with Twin Boundaries, *Appl. Phy. Letter.*, 2007, **90**, p 151909
25. L. Liu, J. Wang, S.K. Gong, and S.X. Mao, Atomistic Observation of a Crack Tip Approaching Coherent Twin Boundaries, *Scient. Repor.*, 2014, **4**, p 4397
26. C. Deng, and F. Sansoz, Effects of Twin and Surface Facet on Strain-Rate Sensitivity of Gold Nanowires at Different Temperatures, *Phy. Rev. B*, 2010, **81**, p 155430
27. C. Deng, and F. Sansoz, Size-Dependent Yield Stress in Twinned Gold Nanowires Mediated by Site-Specific Surface Dislocation Emission, *Appl. Phy. Letter.*, 2009, **95**, p 091914
28. Y.T. Zhu, X.L. Wu, X.Z. Liao, J. Narayan, L.J. Kecskés, and S.N. Mathaudhu, Dislocation–Twin Interactions in Nanocrystalline fcc Metals, *Acta Mater.*, 2011, **59**, p 812–821
29. Z. Yang, L. Zheng, Y. Yue, and Z. Lu, Effects of Twin Orientation and Spacing on the Mechanical Properties of Cu Nanowires, *Scient. Repor.*, 2017, **7**, p 10056
30. S.H. Kim, J.H. Park, H.K. Kim, J.P. Ahn, D.M. Whang, and J.C. Lee, Twin Boundary Sliding in Single Crystalline Cu and Al Nanowires, *Acta Mater.*, 2020, **196**, p 69–77
31. D. Wei, M. Zaiser, Z. Feng, G. Kang, H. Fan, and X. Zhang, Effects of Twin Boundary Orientation on Plasticity of Bicrystalline Copper Micropillars: A Discrete Dislocation Dynamics Simulation Study, *Acta Mater.*, 2019, **176**, p 289–296
32. Y. Zhang, Y. Hou, H. Zheng, L. Zhao, S. Jia, K. Li et al., Effects of Twin Orientation and Twin Boundary Spacing on the Plastic Deformation Behaviors in Ni Nanowires, *j. Mater. Sci. Tech.*, 2023, **135**, p 231–240
33. R. Singh, V. Ajay, and A. Shrivastava, Insights into Fatigue Crack Propagation Behaviour of WAAM Produced SS316 Stainless Steel: Molecular Dynamics Simulation and Experimental Analysis, *Engg. Fail. Ana.*, 2024, **165**, p 108754
34. J. Cui, L. Ma, G. Chen, N. Jiang, P. Ke, Y. Yang et al., Effect of Twin Boundaries on the Strength of Body-Centered Cubic Tungsten Nanowires, *Mater. Sci. Eng.: A*, 2023, **862**, p 143826
35. F. Duan, Q. Li, Z. Shen, Z. Jiang, W. Liu, Y. Yan et al., Anisotropic Mechanical Properties and Deformation Mechanisms of Nanotwinned Ni and Ni Alloys with Extremely Fine Twin Boundary Spacings, *Acta Mater.*, 2023, **260**, p 119311
36. Y. Zhao, H. Cao, and S. Liu, The Dislocation-Based Fatigue Deformation Mechanism of a RAFM Steel under Multi-Axial Loadings, *J. Nucl. Mater.*, 2022, **558**, p 153324
37. D. Ouyang, R. Mao, L. Zhang, S. Liang, and J. Song, Study on the Tensile Properties of Al-Zn-Mg Alloy Based on Molecular Dynamics, *Engg. Fail Ana.*, 2024, **155**, p 107752
38. Q. Kan, B. Qiu, X. Zhang, C. Yu, and G. Kang, Thermo-Mechanically Coupled Functional Fatigue of NiTi Shape Memory Alloys under Multiaxial Cyclic Loadings, *Int. J. Fatig.*, 2023, **172**, p 107657
39. Y. Dong, G. Kang, Y. Liu, H. Wang, and X. Cheng, Dislocation Evolution in 316 L Stainless Steel during Multiaxial Ratchetting Deformation, *Mater. Charact.*, 2012, **65**, p 62–72
40. S. Qin, R. McLendon, V. Oancea, and A.M. Beese, Micromechanics of Multiaxial Plasticity of DP600: Experiments and Microstructural Deformation Modeling, *Mater. Sci. Eng.: A*, 2018, **721**, p 168–178
41. D. Mohr, and J. Jacquemin, Large Deformation of Anisotropic Austenitic Stainless-Steel Sheets at Room Temperature: Multi-Axial Experiments and Phenomenological Modeling, *J. Mech. Phy. Solid.*, 2008, **56**(10), p 2935–2956
42. R. Wu, Q. Yin, J. Wang, Q. Mao, X. Zhang, and Z. Wen, Effect of Re on Mechanical Properties of Single Crystal Ni-based Superalloys: Insights from First-Principle and Molecular Dynamics, *J. Alloys Compd*, 2021, **862**, p 158643
43. R. Wu, Y. Zhao, Q. Yin, J. Wang, X. Ai, and Z. Wen, Atomistic Simulation Studies of Ni-Based Superalloys, *J Alloys Compd*, 2021, **855**, p 157355
44. Q. Yin, Y. Lian, R. Wu, L. Gao, S. Chen, and Z. Wen, Effect of the Potential Function and Strain Rate on Mechanical Behavior of the Single Crystal Ni-based Alloys: A Molecular Dynamics Study, *Chin Phys. B.*, 2021, **30**(8), p 080204
45. L. Zhang, H. Xin, D. Zhao, Z. Li, and S. Ma, Effect of Twin Boundary Density on Mechanical Behavior of Al0.1CoCrFeNi High-Entropy Alloy by Molecular Dynamics Simulation, *Front. Mater.*, 2022, **9**, p 849051

46. S. Nandi, and S. Kumar, Atomistic Structural Transformation of Iron Single Crystal under Bi-Axial Stretching using Classical Molecular Dynamics Simulation, *Bullet. Mater. Sci.*, 2022, **45**(4), p 252
47. S. Kumar, and S.K. Pattanayek, Effect of Multiaxial Tensile Deformation on the Mechanical Properties of Semiflexible Polymeric Samples, *J. Phys. Chem. B*, 2019, **6123**(43), p 9238–9249
48. S. Kumar, Spreading and Orientation of Silver Nano-Drops over a Flat Graphene Substrate: An Atomistic Investigation, *Carbon*, 2018, **138**, p 26–41
49. S. Kumar, and S.K. Das, Characterization of Mechanical Properties and Nano-Porous Structure of Aluminium-Magnesium Alloy during Multi-Axial Tensile Deformation: An Atomistic Investigation, *J. Alloy. Compd.*, 2018, **740**, p 626–638
50. S. Kumar, and S.K. Das, A Triaxial Tensile Deformation-Induced Nanoporous Structure of Aluminium: Estimation of Surface Area, Solid Volume, and Dimensionless Aspect Ratio, *Phy. Chem. Chem. Phy.*, 2017, **19**(31), p 21024–21032
51. S. Kumar, S. Nandi, S.K. Pattanayek, M. Madan, B. Kaushik et al., Atomistic Characterization of Multi Nano-Crystal Formation Process in Fe–Cr–Ni Alloy during Directional Solidification: Perspective to the Additive Manufacturing, *Mater. Chem. Phy.*, 2023, **308**, p 128242
52. S.K. Paul, S. Kumar, and S. Tarafder, Effect of Loading Conditions on Nucleation of Nano Void and Failure of Nanocrystalline Aluminum: An Atomistic Investigation, *Eng. Fract. Mech.*, 2017, **176**, p 257–262
53. M.W. Finnis, and J.E. Sinclair, A Simple Empirical N-body Potential for Transition Metals, *Phil. Mag. A*, 1984, **50**(1), p 45–55
54. X.W. Zhou, M.E. Foster, and R.B. Sills, An Fe-Ni-Cr Embedded Atom Method Potential for Austenitic and Ferritic Systems, *J. Comput. Chem.*, 2018, **39**, p 2420–2431
55. W.G. Hoover, H.A. Posch, B.L. Holian, M.J. Gillan, M. Mareschal, and C. Massobrio, Dissipative Irreversibility From Nosé's Reversible Mechanics, *Mol. Sim.*, 1987, **1**(1–2), p 79–86
56. S. Nose, Constant-Temperature Molecular Dynamics, *J. Phy.: Cond. Matter.*, 1990, **2**, p SA115
57. S. Kumar, and S.K. Pattanayek, Effect of Multiaxial Tensile Deformation on the Mechanical Properties of Semiflexible Polymeric Samples, *J. Phy. Chem. B*, 2019, **123**(43), p 9238–9249
58. S. Plimpton, Fast Parallel Algorithms for Short-Range Molecular Dynamics, *J. Comp. Phy.*, 1995, **117**, p 1–19
59. A. Stukowski, Visualization And Analysis Of Atomistic Simulation Data with OVITO–the Open Visualization Tool, *Model. Simul. Mater. Sci. Eng.*, 2009, **18**(1), p 015012
60. A. Stukowski, Structure Identification Methods for Atomistic Simulations of Crystalline Materials, *Model. Simul. Mater. Sci. Eng.*, 2012, **20**(4), p 045021
61. I.A. Filot, M.P. van Etten, D.W. Trommelen and E.J. Hensen, Bramble: Adaptive Common Neighbor Analysis (CNA) for the Recognition of Surface Topologies in Nanoparticles, *J. Ope. Sour. Soft.*, 2023, **8**(89), p 5710
62. B. Li, Z. Zhang, X. Zhou, M. Liu, and Yu. Jie, Mechanical Behavior and Microstructure Evolution of Al/AlCu Alloy Interface, *J. Mater. Sci.*, 2023, **58**(12), p 5489–5502
63. X. Bin, X. Wang, Y. Fan, and R. Li, Atomistic Investigation on the Strengthening Mechanism of Single Crystal Ni-Based Superalloy under Complex Stress States, *Metal.*, 2022, **12**(5), p 889
64. C. Mieszczynski, P. Jozwik, K. Skrobas, K.S. Skrobas, R. Ratajczak, J. Jagielski, F. Garrido et al., Combining MD-LAMMPS and MC-McChasy2 codes for dislocation simulations of Ni single crystal structure, *Nucl. Inst. Method. Phys. Res. Sect. B: Beam Interac. Mater. Atoms.*, 2023, **540**, p 38–44
65. Y. Zhang, S. Jiang, X. Zhu, and Y. Zhao, Dislocation Mechanism of Void Growth at Twin Boundary of Nanotwinned Nickel Based on Molecular Dynamics Simulation, *Phys. Letter. A*, 2016, **380**(35), p 2757–2761
66. B. Li, and C. Mi, On the Ductile Damage of Nanotwinned Copper Crystal with Prolate Void Defect at the Twin Boundary, *Res. Phys.*, 2019, **14**, p 102464
67. X.A. Hong, G.W. Liu, A. Orozco-Caballero, and J.Q. Fonseca, Effect of Pre-Existing Twinning on Strain Localization during Deformation of a Magnesium Alloy, *Mater. Letters*, 2017, **209**, p 94–96
68. H. Zhang, M. Yang, M. Hou, L. Wang, Q. Zhang, J. Fan, W. Li, H. Dong, S. Liu and B. Xu, Effect of Pre-Existing 101 2 Extension Twins on Mechanical Properties, Microstructure Evolution and Dynamic Recrystallization Of AZ31 Mg Alloy During Uniaxial Compression, *Mater. Sci. Eng. A*, 2019, **744**, p 456–470
69. Y. Xue, H. Sun, N. Feng, C. Kang, L. Yuan, and B. Gan, Effects of Pre-Existing Twins on the Mechanical Properties of Laves Phase V2Hf-Based Alloy, *Mater. Charact.*, 2023, **195**, p 112508

Publisher's Note Springer Nature remains neutral with regard to jurisdictional claims in published maps and institutional affiliations.

Springer Nature or its licensor (e.g. a society or other partner) holds exclusive rights to this article under a publishing agreement with the author(s) or other rightsholder(s); author self-archiving of the accepted manuscript version of this article is solely governed by the terms of such publishing agreement and applicable law.